

Correction

ENGINEERING, APPLIED BIOLOGICAL SCIENCES

Correction for “Regenerative and durable small-diameter graft as an arterial conduit,” by Morgan B. Elliott, Brian Ginn, Takuma Fukunishi, Djahida Bedja, Abhilash Suresh, Theresa Chen, Takahiro Inoue, Harry C. Dietz, Lakshmi Santhanam, Hai-Quan Mao, Narutoshi Hibino, and Sharon Gerecht, which was first published June 10, 2019; 10.1073/pnas.1905966116 (*Proc. Natl. Acad. Sci. U.S.A.* **116**, 12710–12719).

The authors note that the image shown in Fig. 1*D*, *ii* is an inadvertent duplication of an image that was published previously (1). The authors have provided a revised figure that includes the correct image for *ii* in Fig. 1*D*. The corrected figure and its legend appear below. The authors confirm that this change does not alter the interpretation of data or conclusions of the study. The online version has been corrected.

1. S. Zhang et al., Creating polymer hydrogel microfibres with internal alignment via electrical and mechanical stretching. *Biomaterials* **35**, 3243–3251 (2014).

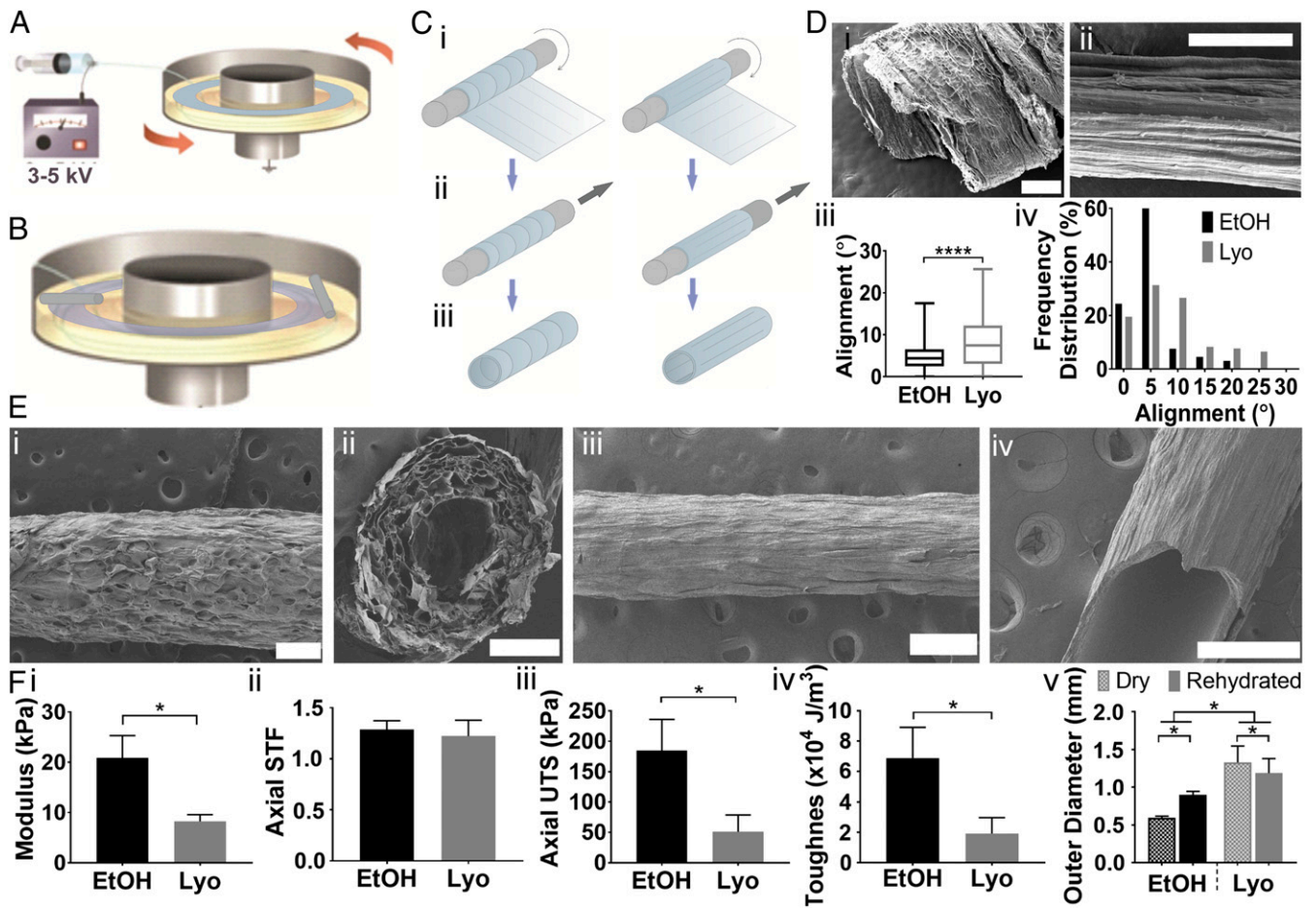


Fig. 1. Fabrication of hollow fibrin hydrogel microfiber tubes. Workflow begins with (A) fibrin hydrogel microfibers being spun into a sheet by rastering the landing position of the biopolymer jet on a rotating collection solution. (B) Sheets are collected by placing a PTFE-coated mandrel on the resultant hydrogel sheet either perpendicular or parallel to the fiber orientation. (C) Sheets are then (i) wrapped, and (ii) the PTFE-coated mandrel is removed after dehydration, (iii) yielding hollow fibrin tubes with circumferential (Left) or longitudinal (Right) alignment. (D) Representative SEM micrographs of (i) circumferentially aligned hollow tube and (ii) a stretch-dried, longitudinally aligned fibrin fiber bundle. Quantification of (iii) longitudinally aligned fibrin microfiber orientation and (iv) orientation distribution for grafts dehydrated via graded EtOH and lyophilization (Lyo) treatments relative to the longitudinal graft axis (0°). (Scale bars: i, 200 μ m; ii, 40 μ m.) (E) Representative longitudinal and cross-section SEM micrographs of (i and ii) Lyo-treated and (iii and iv) EtOH-treated longitudinally aligned hollow tubes. (Scale bar: 400 μ m.) (F) Mechanical properties, including (i) elastic modulus, (ii) axial STF, (iii) axial UTS, (iv) toughness, and (v) outer diameter of fibrin tubes dried using the Lyo and EtOH treatments ($n = 3-5$). * $P < 0.05$; **** $P < 0.0001$.

Published under the [PNAS license](https://www.pnas.org/licenses/pnas-license).

Published September 2, 2021.

www.pnas.org/cgi/doi/10.1073/pnas.2113562118



Regenerative and durable small-diameter graft as an arterial conduit

Morgan B. Elliott^{a,b,c}, Brian Ginn^{c,d,e}, Takuma Fukunishi^f, Djahida Bedja^g, Abhilash Suresh^{a,c}, Theresa Chen^{b,c}, Takahiro Inoue^f, Harry C. Dietz^{g,h,i,j}, Lakshmi Santhanam^k, Hai-Quan Mao^{a,c,d,e}, Narutoshi Hibino^{c,f}, and Sharon Gerecht^{a,b,c,d,l,1}

^aDepartment of Biomedical Engineering, Johns Hopkins University School of Medicine, Baltimore, MD 21205; ^bDepartment of Chemical and Biomolecular Engineering, Johns Hopkins University Whiting School of Engineering, Baltimore, MD 21218; ^cInstitute for NanoBioTechnology, Johns Hopkins University, Baltimore, MD 21218; ^dDepartment of Materials Science and Engineering, Johns Hopkins University Whiting School of Engineering, Baltimore, MD 21218; ^eTranslational Tissue Engineering Center, Johns Hopkins University School of Medicine, Baltimore, MD 21231; ^fDivision of Cardiac Surgery, Department of Surgery, Johns Hopkins University School of Medicine, Baltimore, MD 21205; ^gDepartment of Medicine, Johns Hopkins University School of Medicine, Baltimore, MD 21205; ^hDepartment of Pediatrics, Johns Hopkins University School of Medicine, Baltimore, MD 21205; ⁱInstitute of Genetic Medicine, Johns Hopkins University School of Medicine, Baltimore, MD 21205; ^jHoward Hughes Medical Institute, Chevy Chase, MD 20815; ^kDepartment of Anesthesiology and Critical Care Medicine, Johns Hopkins University School of Medicine, Baltimore, MD 21205; and ^lDepartment of Oncology, Johns Hopkins University School of Medicine, Baltimore, MD 21205

Edited by Robert Langer, Massachusetts Institute of Technology, Cambridge, MA, and approved May 15, 2019 (received for review April 19, 2019)

Despite significant research efforts, clinical practice for arterial bypass surgery has been stagnant, and engineered grafts continue to face postimplantation challenges. Here, we describe the development and application of a durable small-diameter vascular graft with tailored regenerative capacity. We fabricated small-diameter vascular grafts by electrospinning fibrin tubes and poly(ϵ -caprolactone) fibrous sheaths, which improved suture retention strength and enabled long-term survival. Using surface topography in a hollow fibrin microfibrillar tube, we enable immediate, controlled perfusion and formation of a confluent endothelium within 3–4 days in vitro with human endothelial colony-forming cells, but a stable endothelium is noticeable at 4 weeks in vivo. Implantation of acellular or endothelialized fibrin grafts with an external ultrathin poly(ϵ -caprolactone) sheath as an interposition graft in the abdominal aorta of a severe combined immunodeficient Beige mouse model supports normal blood flow and vessel patency for 24 weeks. Mechanical properties of the implanted grafts closely approximate the native abdominal aorta properties after just 1 week in vivo. Fibrin mediated cellular remodeling, stable tunica intima and media formation, and abundant matrix deposition with organized collagen layers and wavy elastin lamellae. Endothelialized grafts evidenced controlled healthy remodeling with delayed and reduced macrophage infiltration alongside neo vasa vasorum-like structure formation, reduced calcification, and accelerated tunica media formation. Our studies establish a small-diameter graft that is fabricated in less than 1 week, mediates neotissue formation and incorporation into the native tissue, and matches the native vessel size and mechanical properties, overcoming main challenges in arterial bypass surgery.

small-diameter vascular graft | infrarenal abdominal aorta mouse model | electrospinning | hydrogel | endothelial colony-forming cells

There is a significant need for small-diameter vascular grafts (sdVGs; <6 mm in diameter) for the treatment of various arterial complications, such as coronary artery disease (CAD) and pediatric congenital cardiovascular defects (CCDs). CAD is the leading cause of death or impaired quality of life, resulting in more than half a million coronary artery bypass surgeries per year (1–4). Meanwhile, pediatric CCDs are present in 1% of live births (5), with most cases requiring repeated surgical reconstruction to maximize long-term survival (5–7). A standard treatment is the use of autologous tissue as a bypass graft (1), but it requires a secondary surgical site to harvest the donor graft and often, has insufficient availability in patients with widespread atherosclerotic vascular disease or previously harvested vessels, ultimately limiting autologous tissue reconstruction (5, 8, 9). Clinical studies have shown that ~15% of autologous vessels used in CAD bypass procedures were

completely occluded or diffusely narrow within 1 y, which is an indicator of long-term survival (10), and 25% of pediatric patients who underwent the Fontan operation had thromboembolic events, despite taking anticoagulants (11). Artificial grafts made of Goretex, Dacron, and polyurethanes are the most common for vascular bypass surgeries that require grafts greater than 6 mm in diameter, but synthetic polymer sdVGs have yet to show clinical effectiveness (12). In fact, the use of synthetic polymer vascular grafts in pediatric CCD procedures remains the leading source of morbidity and mortality (5, 13).

While several efforts have been successful in developing sdVGs (14–20), a functional graft has remained elusive due to post-implantation challenges, including thrombogenicity, decreased elasticity, decreased compliance, aneurysmal failure, calcification, and intimal hyperplasia (11, 14, 18, 21). Design of a biodegradable sdVG that matches the native vessel size and mechanical properties, integrates into the patient's vascular tissue, has low thrombogenicity, and exhibits a clinically relevant shelf life would provide substantial benefits to pediatric cardiothoracic applications by permitting growth with the patient, improving patient morbidity, and reducing long-term costs (1, 16, 21).

Significance

Clinical practice for arterial bypass surgery continues to use autologous vascular tissue harvested from the patient as the gold standard. A functional graft has remained elusive due to post-implantation challenges, including thrombogenicity, mismatched mechanical properties, aneurysmal failure, calcification, and intimal hyperplasia. Many promising graft designs require extensive and complex preparation techniques that impede commercial and clinical translation. Here, we describe the development of acellular off-the-shelf and endothelialized small-diameter vascular grafts in less than 1 week. We establish a durable graft with tailored regenerative capacity that overcomes many post-implantation challenges of arterial bypass grafts.

Author contributions: M.B.E., B.G., T.F., H-Q.M., N.H., and S.G. designed research; M.B.E., B.G., T.F., D.B., A.S., T.C., and T.I. performed research; H.C.D. contributed new reagents/analytic tools; M.B.E., B.G., D.B., A.S., T.C., L.S., H-Q.M., N.H., and S.G. analyzed data; and M.B.E., B.G., H.C.D., L.S., H-Q.M., N.H., and S.G. wrote the paper.

Conflict of interest statement: M.B.E., B.G., H-Q.M., and S.G. have filed intellectual property related to this work through Johns Hopkins Technology Ventures.

This article is a PNAS Direct Submission.

Published under the PNAS license.

¹To whom correspondence may be addressed. Email: gerecht@jhu.edu.

This article contains supporting information online at www.pnas.org/lookup/suppl/doi:10.1073/pnas.1905966116/-DCSupplemental.

Published online June 10, 2019.

Attempts to fabricate natural polymer-derived sdVGs have historically been plagued by limited mechanical properties (22, 23). A widespread method to improve mechanical properties of grafts is the incorporation of vascular smooth muscle cells (vSMCs) and fibroblasts that deposit extracellular matrix (ECM) molecules, including collagen and elastin, before implantation (22, 24, 25), a decellularized example of which is proceeding through clinical trials (26). Similarly designed molded fibrin grafts with encapsulated cells have been implanted in ovine models for up to 6 mo (24, 27–29). These grafts typically require culture for 1–2 mo before implantation, making them difficult to use as an off-the-shelf solution. Aper et al. (28) avoided this preculture step by compacting cellularized fibrin via centrifugation and incorporating Factor XIII cross-linking. Their graft could be immediately implanted but only had a burst pressure of 230 mmHg, significantly less than the burst pressure of a comparably sized human vessel (22, 30). Decellularization takes the full cellularization fabrication technique a step further to reduce immunogenicity and improve use as an off-the-shelf product. A molded fibrin graft seeded with fibroblasts and decellularized after 2 mo of culture has been shown to grow with young lambs and withstand implantation as an arteriovenous bypass in baboons (31, 32). Although requiring extensive and complex preparation, this decellularized sdVG has yielded exciting large animal results. In a similar effort to use cells to modify and enhance the scaffold, Kristofik et al. (33) have used a decellularized vessel as a scaffold to grow thrombospondin-2 knockout cells, which deposit an antithrombotic and promigratory ECM, before decellularizing again for implantation.

Another sdVG fabrication method that is gaining widespread use is the combination of synthetic and natural polymers in a hybrid graft, typically via electrospinning (22, 34–36). For example, Ju et al. (36) combined poly(ϵ -caprolactone) (PCL) and collagen to provide increased mechanical strength and improve cellular infiltration, respectively. With cellularization using vSMCs and endothelial cells (ECs), fabrication took a few weeks and showed significant host integration over 6 mo in an ovine model (36). One potential concern is the level of calcification caused by the different polymers and glutaraldehyde cross-linking after extended implantation of these hybrid sdVGs (37). In addition, their off-the-shelf, acellular, hybrid sdVG failed within 10 d due to thrombosis (36). Many groups incorporate mature fibrin into hybrid grafts to take advantage of its

nonthrombogenic nature (38) along with the improved elastogenesis and host cell integration qualities (29, 39). A fibrin–collagen sdVG had moderately improved mechanical properties relative to fibrin-only molded structures (38). Fibrin and poly(L/D)lactide hybrid grafts seeded with autologous cells were successfully implanted in an ovine model for up to 6 mo, although they still required a month of preculture (40). Significant progress has been made toward the use of natural polymers in sdVGs by incorporating cellularized structures and hybrid materials; however, continued work toward reduced preparation times and a viable off-the-shelf model is needed.

Here, we establish a natural polymer-derived, immediately perfusable sdVG. Controlled surface topography in a hollow fibrin microfiber tube guided the formation of a confluent endothelium *in vitro* and *in vivo*, and the entire structure was fabricated in less than 1 wk. Implantation of acellular or endothelialized cross-linked fibrin grafts with an external ultrathin PCL fibrous sheath in the mouse abdominal aorta supported normal blood flow and vessel patency for 24 wk. Mechanical properties of the implanted fibrin–PCL sheath sdVGs more closely approximated the native abdominal aorta within 1 wk *in vivo*. Neotissue formation was enhanced by endothelialization and mediated by the fibrin layer over time. Overall, we show that our sdVG matches the native vessel size and mechanical properties, incorporates into the native vascular tissue, and has low thrombogenicity.

Results and Discussion

Development of Natural Polymer Conduits with Controlled Surface Topography. To develop an sdVG, we fabricated a fibrin hydrogel microfiber (41–43) as a hollow conduit. Here, we designed an internal stratum that exhibits a microscale, longitudinally aligned surface topography via electromechanical stretching. We hypothesized that the hollow lumen of these tubes would promote immediate implantation and rapid endothelialization of acellular grafts or *in vitro* endothelialization with application of fluid flow through the graft before implantation. To fabricate hollow microfiber tubes, we first electrospun a fibrin sheet with controlled microtopography and then wrapped the aligned microfiber sheets onto polytetrafluoroethylene (PTFE)-coated stainless steel mandrels (Fig. 1 *A* and *B* and *SI Appendix, Fig. S1A*) (37). Wrapping the fibrin sheets with their alignment perpendicular to the mandrel's axis resulted in a circumferentially oriented microtopography, while keeping the alignment axis of

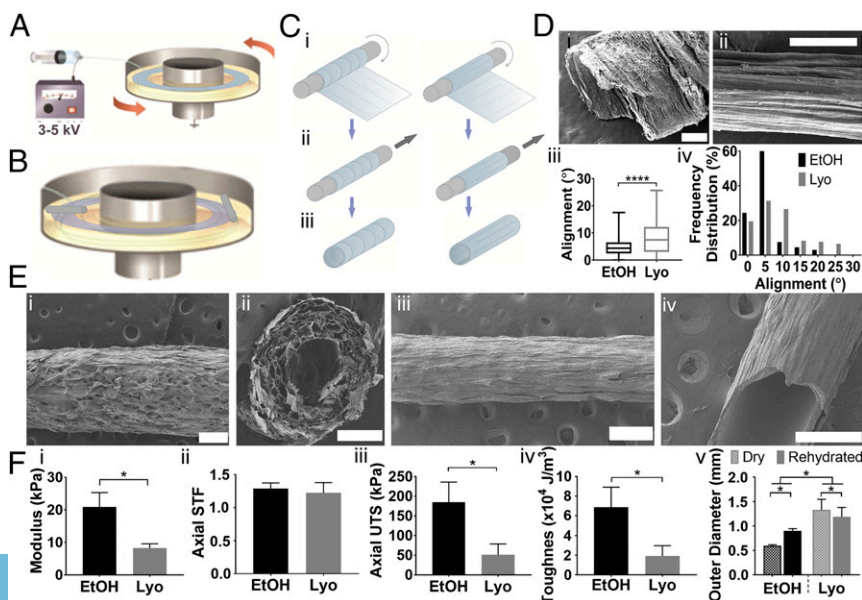


FIG. 1. Fabrication of hollow fibrin hydrogel microfiber tubes. Workflow begins with (A) fibrin hydrogel microfibers being spun into a sheet by rastering the landing position of the biopolymer jet on a rotating collection solution. (B) Sheets are collected by placing a PTFE-coated mandrel on the resultant hydrogel sheet either perpendicular or parallel to the fiber orientation. (C) Sheets are then (i) wrapped, and (ii) the PTFE-coated mandrel is removed after dehydration, (iii) yielding hollow fibrin tubes with circumferential (Left) or longitudinal (Right) alignment. (D) Representative SEM micrographs of (i) circumferentially aligned hollow tube and (ii) a stretch-dried, longitudinally aligned fibrin fiber bundle. Quantification of (iii) longitudinally aligned fibrin microfiber orientation and (iv) orientation distribution for grafts dehydrated via graded EtOH and lyophilization (Lyo) treatments relative to the longitudinal axis (0°). (Scale bars: i, 200 μ m; ii, 40 μ m.) (E) Representative longitudinal and cross-section SEM micrographs of (i and ii) Lyo-treated and (iii and iv) EtOH-treated longitudinally aligned hollow tubes. (Scale bar: 400 μ m.) (F) Mechanical properties, including (i) elastic modulus, (ii) axial STF, (iii) axial UTS, (iv) toughness, and (v) outer diameter of fibrin tubes dried using the Lyo and EtOH treatments ($n = 3-5$). * $P < 0.05$; **** $P < 0.0001$.

the fibrin sheets parallel to the mandrel's axis resulted in longitudinally aligned microtopography (Fig. 1 C and D i and ii). After wrapping, microfiber sheets were dehydrated by being frozen and lyophilized or by stepwise dehydration with ethanol (EtOH) and subsequent air drying for easy removal of the mandrel from resulting hollow fibrin microfiber tubes. The graded EtOH dehydration improved maintenance of microfiber alignment definition as shown by the longitudinal microfibrils being oriented closer to the axial direction of the graft (0°) and having a narrower frequency distribution of microfiber alignment (Fig. 1 D, iii and iv). Lyophilized microfiber tubes had a highly porous internal structure after removal of water, but tube walls were very thick (Fig. 1 E, i and ii). Graded EtOH dehydration reduced wall thickness to several hundred micrometers and increased microfiber density due to material compaction (Fig. 1 E, iii and iv and SI Appendix, Fig. S1). The graded EtOH dehydration process resulted in improved tube elastic moduli, axial ultimate tensile stress (UTS), and toughness; reduced tube diameters in both dry and rehydrated states; and maintained similar axial strain to failure (STF) relative to the lyophilized tubes (Fig. 1F). These improved mechanical properties are due to the physical cross-linking from compaction of the fibrin microfiber sheets within the hydrogel tube, which also allows for

the formation of hydrogen bonds throughout the hydrogel as it is dehydrated (SI Appendix, Fig. S1) (44, 45). Given the enhanced surface texture control and mechanical properties of the graded EtOH dried tubes, this dehydration method was used for all subsequent graft fabrication and testing. Graft dehydration will enable storage before use, yielding an off-the-shelf, acellular sdVG.

Immediate Perfusion and Mechanical Endurance. To test construct integrity before transplantation, we first examined perfusion through the fibrin sdVG. We encased the grafts in a single-chamber bioreactor. Several bioreactors were set up in parallel to enable multiple sdVGs to be tested simultaneously (Fig. 2A). Grafts of varying lengths and diameters can be cultured in this bioreactor system by altering the length and gauge of the needle, respectively, used to cannulate the fibrin microfiber tube. We assessed media perfusion through the acellular sdVG with the pulsatile perfusion system at various physiologic shear stresses, an important mechanosensation for ECs and their subsequent recruitment of mural cell populations (46, 47). Vascular shear stress can range between 1 and 70 dyn/cm² depending on the size and type of vessel (48), with moderate levels (5–10 dyn/cm²) being prevalent in arteries and high levels (>10 dyn/cm²) being present in capillaries and small arterioles (49, 50). To definitively

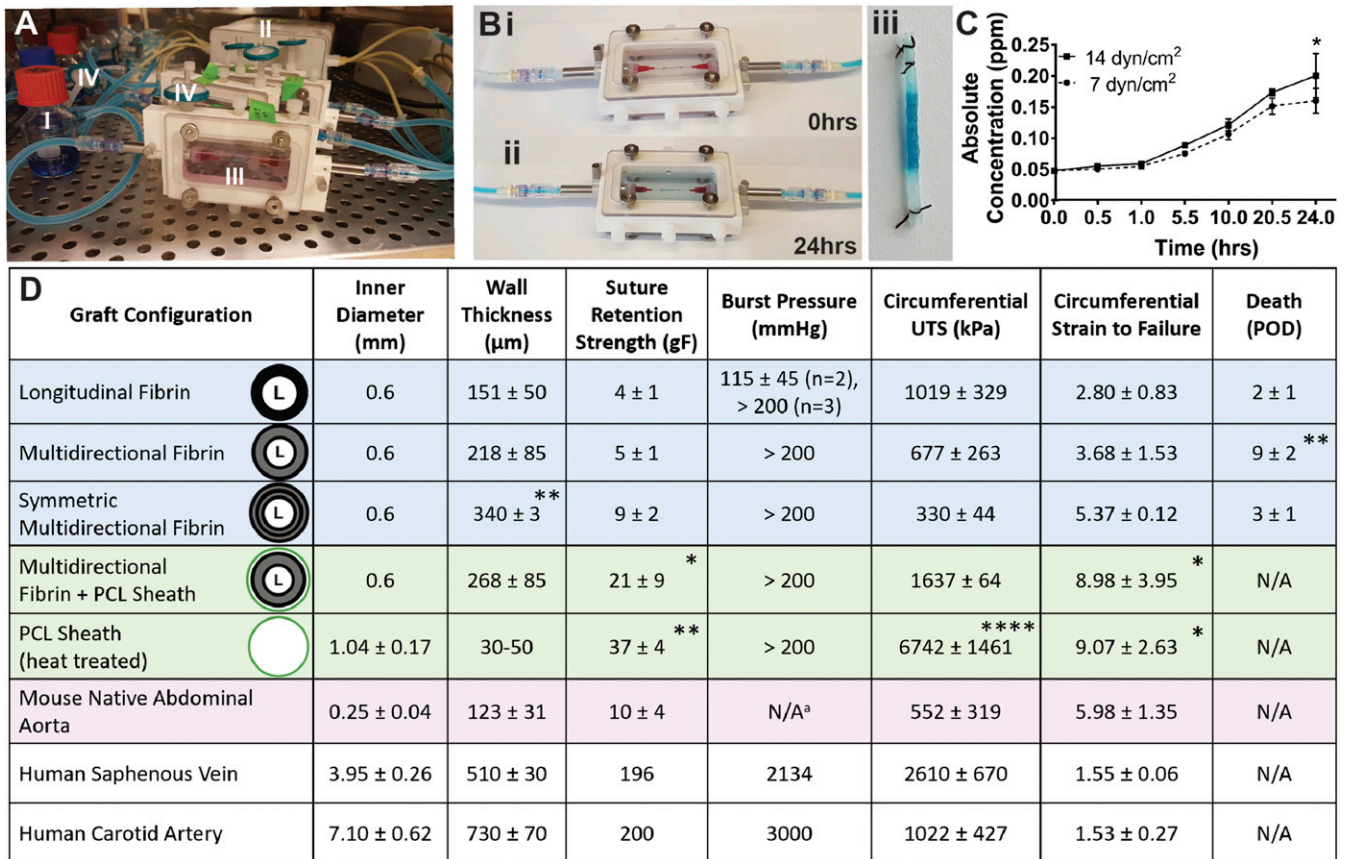


Fig. 2. In vitro perfusion, mechanical testing, and optimization of fibrin conduits. (A) The parallel perfusion system features (I) media reservoirs, (II) a peristaltic pump, (III) up to four LumeGen chambers, and (IV) air filters for gas exchange. Grafts were ligated with sutures around the cannulae and pre-perfused with blue dye to ensure that no leaks from ligations occurred. (B) sdVGs in the PBS-filled bioreactor (i) before perfusion and (ii) in a chamber tinted blue after 24 h of perfusion with a shear stress of 14 dyn/cm². (iii) A magnified view of the fibrin microfiber tube after perfusion. (C) Average absolute dye concentration in the chamber over 24 h for acellular fibrin microfiber tubes exposed to pulsatile flow at low and high shear stresses (n = 3–5). *P < 0.05 between acellular grafts at 24 h. (D) Mechanical properties of various graft configurations and controls. Graft configuration diagrams indicate the combinations of longitudinally (black) and circumferentially (gray) wrapped microfiber sheets around the lumen (L) as well as the PCL sheath (green; not to scale). Human vessel values provided as reference for large animal model relevance (22, 30, 88–90). ^aNot applicable (N/A): Burst pressure could not be collected for the native mouse abdominal aorta, as it had too many branches to be stably pressurized during pressure myography; death after implantation occurred significantly later for the multidirectional graft group (n = 3–6). *P < 0.05; **P < 0.01; ****P < 0.0001.

reveal any perfusion issues, phosphate buffered saline (PBS) with blue dye was flowed through the fiber at shear stresses of 7 or 14 dyn/cm², while clear PBS was used to fill the chamber (Fig. 2 B, *i*), which would drastically change color from leaks. Before perfusion, blue dye was injected into the lumen to ensure that no leaks from the ligation point around the graft and needles occurred. Perfusion for 24 h at 7 and 14 dyn/cm² was successful, with no leaks from the fiber. After 24 h of high-shear stress exposure, the PBS-filled chamber was only tinted blue (Fig. 2 B, *ii*). A magnified view of the fibrin microfiber tube after perfusion shows that only the area between the needles was stained blue by the dye (Fig. 2 B, *iii*). Until the 24-h time point, there was no significant difference in the absolute dye concentration in the chamber between the low- and high-shear stress conditions (Fig. 2C). The uniform distribution of blue tint in the chamber and the small overall increase in absolute dye concentration after 24 h showed that only diffusion through the fibrin graft wall occurred and that flow could be maintained. These results confirmed that the hollow fibrin microfiber sdVGs can be immediately perfused, indicating potential for using them as arterial conduits. While we assessed the effects of a range of physiologic shear stresses on graft function, small pulsatile pressures similar to pulmonary artery levels were simulated (51). In the future, larger physiologic pressures should be investigated before implantation.

To demonstrate the compatibility of the grafts for therapeutic use, the acellular fibrin sdVGs with various fibrin microfiber configurations were implanted as abdominal aorta interposition grafts in a murine model (SI Appendix, Fig. S2A). Three types of fibrin grafts were tested: longitudinal graft is composed of 6 or 10 longitudinally aligned fibrin sheets; multidirectional graft is composed of 10–12 multidirectional sheets of fibrin with a pattern of 2 internal longitudinal (0°) sheets, 5–8 central circumferential (90°) sheets, and 2–3 external longitudinal sheets; and symmetric multidirectional graft is composed of 10 symmetrically altering multidirectional fibrin sheets with a pattern of 2 internal, central, and external longitudinal sheets separated by 2 central circumferential sheets (Fig. 2D). All angles are relative to the graft longitudinal axis. Focusing on graft properties (Fig. 2D), it should be noted that, while the inner diameter and wall thickness of the fibrin grafts were larger than the native mouse abdominal aorta, only the symmetric multidirectional graft had significantly thicker walls than the native vessel. The small-native diameter and wall-thickness values may be attributed to the relatively small size of female severe combined immunodeficient (SCID) Beige mice at 8–10 wk of age and the use of the distal abdominal aorta for histology measurements. Significantly relevant to our initial in vivo results, it was found that all fibrin graft groups had a decreased suture retention strength (SRS) relative to the native mouse aorta. Multidirectional and symmetric multidirectional grafts had burst pressures greater than 200 mmHg, larger than the longitudinal graft group. Due to limitations of the pressure myograph system, we were unable to pressurize the vessels above 200 mmHg, but the data collected indicate that the grafts should have burst pressures relevant to mouse physiology (52). We next assessed circumferential UTS and STF, which normalize forces to the sample dimensions. We found no significant difference in fibrin graft and native abdominal aorta circumferential UTS and STF, indicating similar mechanical properties to the native tissue. To understand the global mechanical response behavior of the fibrin grafts, the compliance and axial properties were also assessed (SI Appendix, Table S1). Axial electromechanical microfiber alignment in the longitudinal graft yielded larger axial UTS and STF, indicating that alignment variation changes overall sdVG mechanics. Based on these data, we hypothesized that the multidirectional fibrin graft would perform best in vivo.

Immediately after implantation, no significant difference in the normalized mean blood flow through the various grafts was detected (SI Appendix, Fig. S2B), indicating that grafts were able

to withstand initial high-pressure arterial flow and did not lose patency. However, longitudinal grafts failed on postoperative day (POD) 2 ± 1 ($n = 5$), with most rupturing from a tear in the fibrin wall along the longitudinal topography emanating from the sutures (SI Appendix, Fig. S2C). To combat this tearing issue, the fibrin sdVGs were cross-linked with (1-ethyl-3-(3-dimethylaminopropyl)-carbodiimide)/N-hydroxysuccinimide (EDC/NHS). Noncross-linked grafts resulted in death on POD 1 ± 0 ($n = 3$), while cross-linked grafts resulted in a delayed death on POD 3 ± 1 ($n = 2$). EDC/NHS cross-linking has previously been shown to make natural polymer hydrogels resistant to macrophage degradation, improve their mechanical properties, and decrease their swelling ratio (53). Cross-linking the fibrin D-globular domains with EDC/NHS would create D-dimers (SI Appendix, Fig. S1) (44), similar in location to the cross-link typically formed by Factor XIII in vivo (54, 55), thereby creating a hydrogel with delayed degradation that will allow for increased host cell infiltration and remodeling before loss of mechanical stability. Given the slight benefit of cross-linking, all future grafts were cross-linked with EDC/NHS before graded EtOH dehydration (SI Appendix, Fig. S1). While the multidirectional grafts resulted in a significantly increased mouse lifespan, rupture with the same tear propagation pattern from the suture points occurred in 16 of 17 cases with the various fibrin microfiber configurations (SI Appendix, Fig. S2D and Table S2). One mouse died due to graft occlusion (SI Appendix, Table S2). Hematoxylin and eosin (H&E) staining of these sdVGs did not show degradation of the natural polymer fibrin material, which would result in wall thinning, to be the cause of mechanical failure (SI Appendix, Fig. S2E). Mechanical failure from material fatigue and subsequent death led to clotting in the graft lumen. In all cases, the grafts were able to withstand the high-pressure blood flow after the surgical clamps were released and even withstood aortic flow for several days without bursting or leaking, a longer period than previously tested on natural polymer grafts (56). Initial successful in vivo implantation indicates surgical utility of the fibrin microfiber tube. However, over time, these fibrin grafts began to fail due to material fatigue. Adding an electrospun PCL fiber sheath (30- to 50- μ m thick) as a surgical intervention to prevent tearing at the suture sites resulted in a significantly larger SRS for the PCL sheath combined with the multidirectional fibrin graft relative to the fibrin grafts and native mouse abdominal aorta (Fig. 2D). Importantly, the circumferential UTS was significantly larger for the PCL sheath alone but not the multidirectional graft + PCL sheath relative to all other groups (Fig. 2D). Both the PCL sheath and the fibrin-PCL sdVG resulted in improved circumferential STF relative to the longitudinal and multidirectional fibrin grafts. Taken together, while our first group of natural grafts failed due to inadequate mechanical strength, the graft failure caused by suture tearing was resolved by the addition of cross-linking and an ultrathin PCL fibrous sheath as a surgical intervention, allowing us to overcome the mechanical property disadvantages of natural polymer sdVGs (22) and yielding a durable sdVG. Relative to human blood vessels, the PCL-fibrin sdVG has significantly decreased SRS and burst pressures (Fig. 2D), which are critical to successful implant. However, when comparing the circumferential UTS and STF for the saphenous vein, a commonly used vessel in coronary artery bypass procedures (22), with the fibrin-PCL grafts, they have similar strength when normalized to vessel dimensions at failure. This indicates that a scaled-up fibrin-PCL sdVG may have potential for use as a graft in large animal models.

In Vitro and In Vivo Endothelialization. Critical to sdVG applications, longitudinally aligned ECs reduce platelet activation and adhesion, aid in fibrinolysis, and prevent intimal hyperplasia (23, 57–59). Thus, we sought to test whether the natural sdVGs guide rapid endothelialization. The natural sdVG and the bioreactor system enabled us to examine the stepwise development of endothelialized constructs in vitro using an internal seeding of

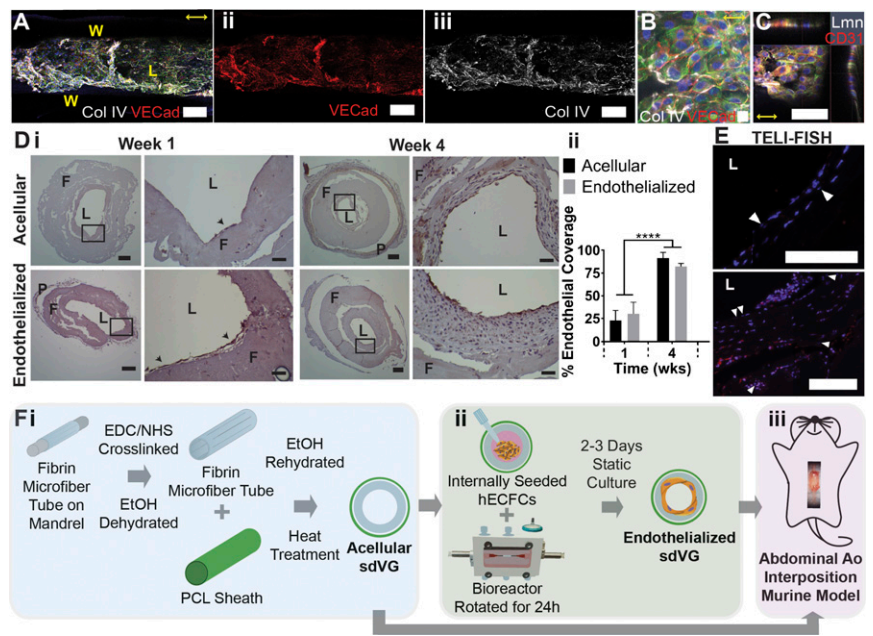
endothelial colony-forming cells (ECFCs) via injection into the luminal space. ECFCs are a subtype of endothelial progenitor cells (EPCs) with high proliferation potential, and thus, they are useful for clinical applications, as they can be found both in umbilical cord blood and circulating in human adult peripheral blood (60–62). After 3–4 d of static ECFC culture, we observed the formation of a confluent endothelium expressing mature endothelial markers vascular endothelial cadherin and CD31 as well as deposition of ECM proteins Collagen IV and laminin (Fig. 3 A–C). The single cell-thick ECFC monolayer recapitulates the tunica intima of native vessels (Fig. 3C). The endothelialized fibrin structures were attained after only 3 d of culture, significantly shorter than other studies that require 1–18 wk of cell culture before implantation (17, 24, 32, 36, 63). Ultimately, hollow fibrin microfiber tubes were able to be immediately perfused and endothelialized, indicating potential for use as arterial conduits.

We next determined tunica intima formation *in vivo*. We compared acellular and endothelialized fibrin–PCL sdVGs implanted as abdominal aorta interposition grafts in an SCID mouse model for 1 and 4 wk. Aspirin was administered at a dose of 3–4 mg/kg per day from the time of implant until harvest. Endothelialization of the luminal surface began by week 1 and significantly increased from week 1 to week 4, reaching complete endothelialization (Fig. 3D). It should be noted that the luminal EC coverage of the endothelialized grafts was not significantly larger than the acellular sdVG coverage. To assess presence of the human ECFCs, we performed fluorescent *in situ* hybridization staining of telomeres (TELI-FISH) using a protein nucleic acid probe for the 1-wk endothelialized group (64). We found that few human cells remained in the graft by week 1, although some human cells remained on the luminal surface and others migrated into the fibrin wall (Fig. 3E, indicated by arrowheads). We did not expect to see significant numbers of human cells present at 1 wk given that previous work with a scaffold wrapped in a pluripotent stem cell-differentiated cell sheet showed that over 50% of cells present at week 1 were host cells (65). However, we speculated that EPCs might have a longer residency given that a previous study showed that preseeded EPCs covered

80 and 10% of the luminal surface of a decellularized porcine vessel scaffold at 2 and 19 wk postimplantation, respectively, in an ovine model (66). Additional investigation is needed to identify whether the implanted human ECFCs were washed away, migrated to other tissues, or underwent apoptosis. Determination of how to prevent implanted cell loss would be critical to clinical translation. Based on these results, we resolved that our final sdVG configuration (Fig. 3F) would include an EDC/NHS cross-linked multidirectional fibrin microfiber tube, an ultrathin PCL sheath, and endothelialization before implantation. Multiple endothelialized and acellular sdVGs can be fabricated within 1 wk, offering a significantly reduced, clinically relevant, and commercially relevant timeline for patient-specific graft fabrication.

Patency and Structural Integrity *In Vivo*. To determine whether ECFCs enhance the function of sdVGs, we compared acellular and endothelialized sdVGs implanted as abdominal aorta interposition grafts in an SCID mouse model for 1, 4, 8, or 24 wk ($n = 3–7$). To assess the functionality of the sdVGs *in vivo*, we quantified blood flow through the grafts with pulse wave Doppler spectrum and speckle contrast imaging technology as well as examined mechanical properties of harvested sdVGs. For a longitudinal assessment of graft function, we used color Doppler to visualize blood flow through the graft and measured blood velocity in the distal aorta before the iliac bifurcation with pulse wave Doppler spectrum (Fig. 4 A, *i* and *ii*). There was no significant difference in peak systolic velocity (PSV), mean velocity (MV), or end diastolic velocity (EDV) between the acellular and endothelialized sdVG groups (Fig. 4 A, *iii*). While EDV was significantly decreased, resulting in a significantly increased resistivity, at 16 wk for the acellular sdVG relative to earlier time points, the flow returned to baseline values. Ultimately, no changes in resistivity index (RI) and pulsatility index (PI) occurred over time in the acellular and endothelialized groups relative to the baseline measurements (Fig. 4 A, *iv*). Therefore, no change in function of the surrounding vasculature as an arterial conduit occurred due to the implantation of the sdVGs. The speckle contrast imaging technology allowed us to

Fig. 3. sdVG endothelialization. (A) Maximum intensity projection of (i) merged, (ii) endothelial (red), and (iii) ECM (white) stains. (Scale bar: 200 μ m.) (B) High-magnification maximum intensity projection. (Scale bar: 20 μ m.) (C) Orthogonal projection of endothelialized fibrin sdVGs at days 3–4 of culture. F-actin is in green, and nuclei are in blue. Double-headed arrows show microfiber longitudinal direction ($n = 3$). Col IV, Collagen IV; L, lumen; Lmn, laminin; VECad, vascular endothelial cadherin; W, fibrin wall. (Scale bar: 100 μ m.) (D) Representative histological serial sectioning of explanted fibrin–PCL sdVGs. (i) Staining for ECs (CD31) at weeks 1 and 4 to assess tunica intima formation. ECs lining the lumen at week 1 are indicated by arrows. Lumen (L), PCL sheath (P), and fibrin (F) are indicated. Boxes in the low-magnification images (columns 1 and 3) indicate the high-magnification image (columns 2 and 4) locations. (Scale bars: columns 1 and 3, 200 μ m; columns 2 and 4, 30 μ m.) (ii) Quantification of EC coverage of the luminal surface ($n = 3–6$). **** $P \leq 0.0001$. (E) TELI-FISH in endothelialized grafts explanted at week 1 indicates mouse cells with red-labeled telomeres, while human telomeres do not fluoresce. Arrowheads indicate human cells. (Scale bar: 100 μ m.) (F) Workflow schematic for fabrication of sdVGs, which were used for all subsequent experiments, involving (i) electrospinning of fibrin tubes and PCL sheaths, (ii) endothelialization of grafts with human endothelial colony-forming cells (hECFCs) to form a tunica intima before implantation, and (iii) implantation of acellular or endothelialized sdVGs in the abdominal aorta of an SCID mouse model.



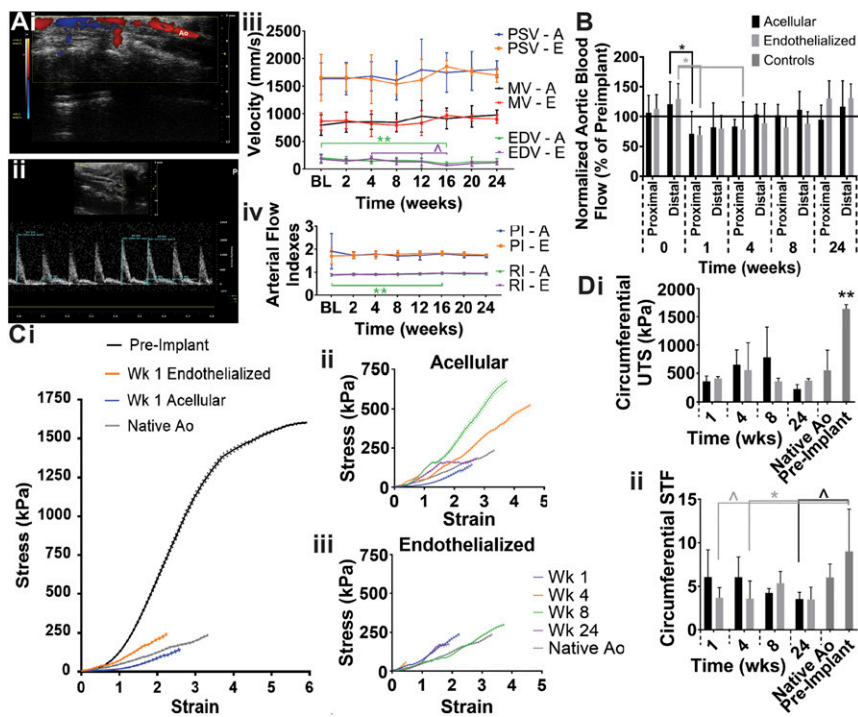


Fig. 4. Maintenance of patency and mechanical properties for up to 24 wk in vivo. (A, *i*) Color Doppler was used to visualize flow through the abdominal aorta (Ao) and graft. (A, *ii*) The pulse wave Doppler spectrum was used to measure the (A, *iii*) PSV, EDV, and MV of the blood in the distal abdominal aorta. (A, *iv*) No significant differences in the PI or RI of the surrounding artery were found (BL, baseline; A, acellular; E, endothelialized; $n = 3-20$). (B) Blood flow through the proximal and distal abdominal aorta immediately after implantation (0) or before harvest of the graft was measured with speckle contrast imaging technology and normalized to preimplant flow values for the same mouse ($n = 3-23$). (C) Stress-strain curves (mean \pm standard error of the mean) of the (i) grafts at week 1 relative to controls, (ii) acellular grafts over time, and (iii) endothelialized grafts over time indicate changing elasticity. (D) Ultimate circumferential (i) stress and (ii) strain of the explanted grafts, native abdominal aorta, and fibrin-PCL sdVG at preimplantation ($n = 3-5$). * $P < 0.05$; ** $P \leq 0.01$; $\wedge P \leq 0.07$.

compare flow through the abdominal aorta and graft immediately postimplant (week 0) and preexplant (weeks 1–24) with baseline values of abdominal aorta flow (Fig. 4B). Blood flow through the abdominal aorta spiked immediately postimplantation, was reduced at weeks 1 and 4 for both groups, returned to preimplantation values at week 8, and then, increased slightly at week 24. The steady increase in flow over time may be due to graft remodeling or aging. The lack of significant difference in the flow between the proximal and distal abdominal aorta indicates that no significant occlusion occurred within the sdVGs. This corroborated the pulse wave Doppler spectrum data and indicated that the sdVGs remained patent over time.

After explant of the sdVGs, circumferential stress and strain were measured to determine changes in graft mechanical properties. The stress-strain curves demonstrate that the elasticity of the sdVGs significantly increased by just 1 wk after implantation, indicating remodeling of both grafts toward the native aorta (Fig. 4C, *i*). The stress-strain curve also remodeled from an S-shaped curve toward the more typical exponential curve for a native vessel. Interestingly, the acellular sdVG elasticity consistently decreased over the first 8 wk but then, returned to native elasticity levels at week 24 (Fig. 4C, *ii*); meanwhile, elasticity of the endothelialized grafts closely approximated the native abdominal aorta over all 24 wk (Fig. 4C, *iii*). All explanted grafts, from week 1 to 24, had significantly reduced circumferential UTS relative to the preimplantation sdVG and more closely approximated the native abdominal aorta (Fig. 4D, *i*). The circumferential STF of the endothelialized grafts tended to be smaller than the preimplant grafts at early time points but became more similar to the native and preimplant structure values over time (Fig. 4D, *ii*). Meanwhile, the acellular harvested grafts at week 24 tended to have a decreased circumferential STF relative to the preimplant structure, indicating some remodeling. Overall, the graft circumferential UTS and STF closely approximated the native aorta control. The drastic change in both graft elasticity and circumferential UTS from preimplant to 1 wk postimplant may be due to a wide variety of stimuli in the complex in vivo environment, including but not limited to mechanical stimulation from high pulsatile, aortic flow; neurohumoral and paracrine

signaling; a large variety of cell-type interactions; aqueous environment surrounding the hydrophobic PCL sheath; and enzymatic activity. Ultimately, both the acellular and endothelialized sdVGs were able to maintain patency and functionality as an arterial conduit over 24 wk in vivo while exposed to the high pulsatile pressure of the abdominal aorta.

Cell Infiltration over 24 Wk In Vivo. Cell infiltration leads to graft remodeling and neotissue formation, critical for the long-term graft integration, function, and overall healing of the diseased artery. Neotissue formation was grossly evident by week 24 due to the pink color of the explanted grafts, like the native abdominal aorta, indicating extensive host cell infiltration and remodeling of the originally white scaffolds (Fig. 5A). Host cells migrate across the sdVG luminal surface from the anastomosed native aorta (67), leading to the complete coverage of the fibrin scaffold seen in longitudinal histological sections of the sdVG (Fig. 5A). Progressive fragmentation and remodeling of the fibrin wall over time are evident in the H&E staining (SI Appendix, Fig. S3B). The inner diameter of the endothelialized and acellular sdVGs slightly decreased over time toward the native aorta inner diameter, which was significantly smaller than the preimplant and harvested sdVGs (SI Appendix, Fig. S3C). Unlike the fibrin sdVG, the PCL sheath did not degrade and maintained its thickness (SI Appendix, Fig. S3D), which was not surprising given the slow degradation rate of PCL sdVGs (19).

As the scaffold remodeled, we assessed graft calcification over time, a major limitation of most current synthetic polymer sdVGs (19, 22, 68), using von Kossa staining (Fig. 5B, *i*). By week 8, calcification was significantly increased in the acellular sdVGs relative to the endothelialized sdVGs (Fig. 5B, *ii*). Positive staining of 0.8% or more of the graft cross-sectional area at periodic points throughout the length from the anastomosis point to the midline was defined as evidence of calcification. By this definition, 50% of the acellular grafts at weeks 8 and 24 had evidence of calcification, while none of the endothelialized sdVG

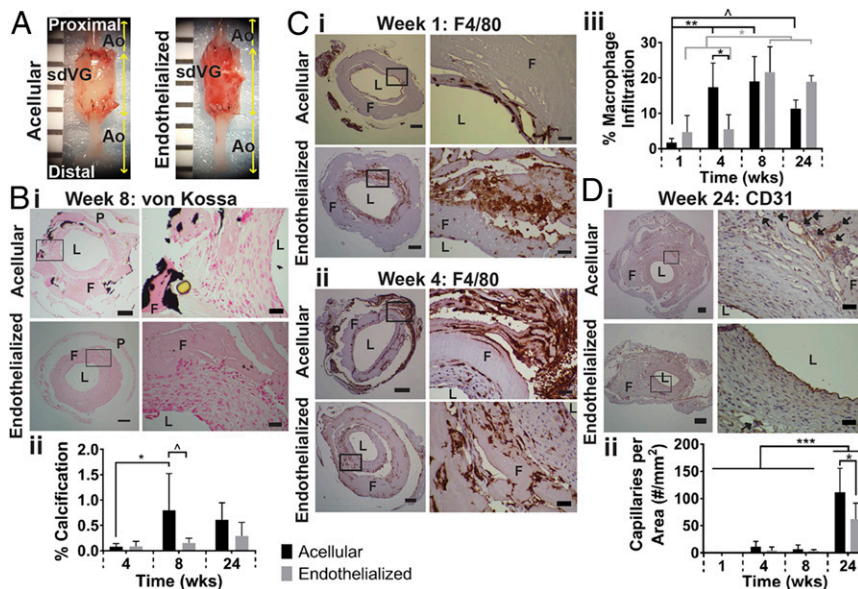


Fig. 5. Cell infiltration and remodeling of fibrin layer with enhanced and controlled regeneration in bioactive, endothelialized sdVG. (A) Acellular and endothelialized sdVG explants anastomosed to native abdominal aorta (Ao) at week 24. (Scale bar: 1-mm marks.) (B) Calcification (von Kossa) (i) staining and (ii) quantification. (C, i and ii) Staining for mature macrophages (F4/80) to assess (C, iii) infiltration in acellular and endothelialized grafts. (D, i) Staining for ECs (CD31) to assess (D, ii) microvasculature formation. Lumen (L), PCL sheath (P), fibrin (F), capillaries (arrows), and fragmented fibrin (asterisks) are indicated. Boxes in the low-magnification images (D, i, Left) indicate the high-magnification image (D, i, Right) locations ($n = 3-6$). (Scale bars: D, i, Left, 200 μm ; D, i, Right, 30 μm). * $P < 0.05$; ** $P \leq 0.01$; *** $P \leq 0.001$; $\wedge P \leq 0.07$.

were indicative. No appreciable calcification of the endothelialized sdVGs could be observed over time (Fig. 5 B, i and SI Appendix, Fig. S3E).

We also examined both overall and specific cell infiltration to understand other differences in neotissue formation. The hematoxylin stain demonstrates slightly more cells infiltrating overall at week 1 in endothelialized sdVGs (422 ± 367 cells) compared with acellular sdVGs (310 ± 179 cells). Given that a few human cells are present at week 1, the increased presence of all cell types indicates infiltration and an acute bioactive effect of endothelialization. To assess the macrophage reaction to the sdVGs, we stained with F4/80 and found that macrophages initially clustered along the lumen (Fig. 5 C, i) but slowly infiltrated throughout the fibrin wall over time (Fig. 5 C, ii and SI Appendix, Fig. S3F). At week 4, the acellular sdVG contained significantly more macrophages than the endothelialized group (Fig. 5 C, iii). Additionally, the endothelialized group had a more controlled, delayed infiltration of macrophages over time. The macrophages may have contributed to remodeling the sdVGs by degrading the fibrin by week 24 (SI Appendix, Fig. S3F). However, limited conclusions can be drawn about the immune response to these sdVGs, as this study was performed in an immunodeficient mouse model due to the use of human ECFCs, and this confounds conclusions about the long-term immune response. Additionally, fibrin has been shown to recruit other host cells in addition to macrophages (69), all of which may be contributing to scaffold remodeling via cell-mediated proteases (70).

We next assessed microvasculature, or vasa vasorum-like structure, formation in the fibrin-media layer of the regenerating artery. Capillaries were occasionally visible in the graft wall by week 4 but became prevalent at week 24 in the medial layer and at the fibrin-media interface, generating neo vasa vasorum-like structures (Fig. 5D). At week 24, the acellular sdVG had significantly more neo vasa vasorum-like structures, as indicated by capillaries per cross-sectional area, than the endothelialized group (Fig. 5 D, ii). As for the macrophage infiltration, the endothelialized group had more controlled microvasculature formation. Ultimately, the fibrin layer appeared to guide macrophage infiltration and neo vasa vasorum-like structure development at the fibrin-media interface, eventually leading to neotissue formation. The *in vitro* endothelialization before implantation seemed to control the rate of these events and reduce calcification over time. In combination with the elasticity of the

endothelialized grafts being more similar to the native artery over time, these results suggest that the endothelialized grafts have a more enhanced and controlled regenerative, or bioactive, effect. Cellular infiltration and remodeling indicate positive neotissue formation in both groups, but to fully understand scaffold remodeling into a functional artery, the tunica media must be examined.

Tunica Media Formation. We next assessed the cellularization of the sdVGs by host smooth muscle cells (SMCs). By week 4, SMCs had formed a medial layer and began to orient themselves circumferentially as shown by the lengthening of cells around the lumen (SI Appendix, Fig. S4A). By week 8, not only was the circumferential SMC orientation more consistent and apparent for both acellular and endothelialized sdVGs but also, the medial layer was significantly thicker in the endothelialized sdVG (Fig. 6A). This indicates the formation of a muscular tunica media with circumferential orientation, which is typically seen in native aorta (23).

We next evaluated ECM remodeling in the grafts. Increased levels of collagen were found to be deposited in the tunica media along the implantation period, reaching a similar structure to the native abdominal aorta by week 24 (Fig. 6B). For both grafts, the collagen composition consistently increased over time, with grafts explanted at weeks 8 and 24 containing significantly more collagen than those explanted at week 1 (Fig. 6C and SI Appendix, Fig. S4B). We then focused on assessing elastin deposition, which would indicate the formation of mature, contractile vasculature with an elastic ECM. We found some deposition of elastin at week 4, which became more organized by week 8 (SI Appendix, Fig. S4C). Although this elastin was not as organized into lamellae as the native elastin, it indicated significant remodeling of the sdVG by host tissue toward a mature, healthy phenotype. The native structure contained distinct, thick elastic bands, while the week 8 elastin fiber structure had a lacey appearance with nodes connecting the thin elastic bands. By week 24, the elastin fibers appeared to be thicker, wavier bands with fewer and more distant nodes connecting the bands, more like the native structure (Fig. 6D).

Formation of the tunica media occurs transanastomotically from the neighboring aorta for the establishment of a continuous lumen with smooth cellular walls that more closely approximate the native lumen. Subsequent remodeling of the fibrin scaffold is shown by the appearance of SMCs and collagen between fragmented pieces of fibrin (Fig. 6E). Ultimately, the compact layering with enhanced distinction of collagen, wavy elastin, and

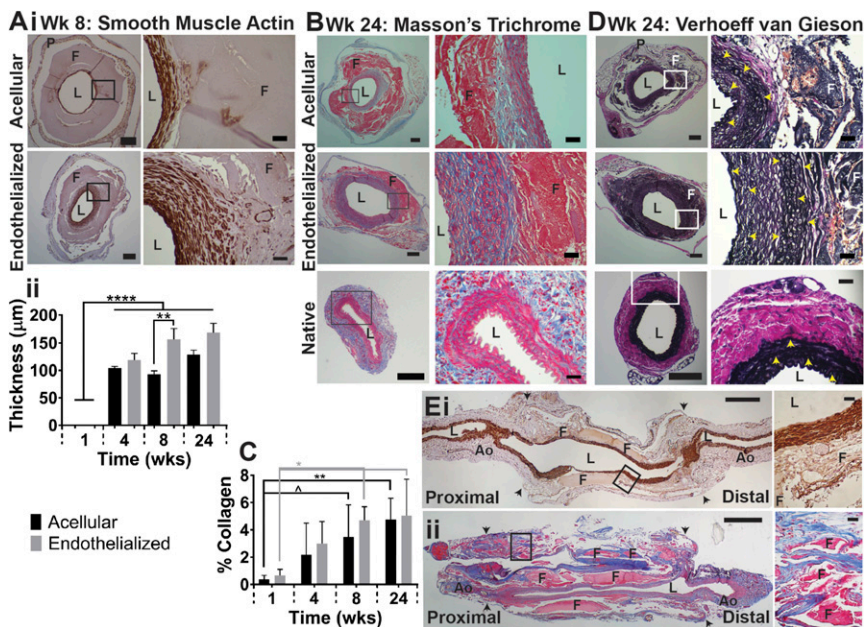


Fig. 6. Tunica media formation resembles native structure by week 24 in acellular and bioactive sdVGs. Representative cross-sectional, histological serial sectioning of explanted acellular and endothelialized sdVGs at 8 and 24 wk postimplantation. Native abdominal aorta serves as control. (A, *i*) Smooth muscle cell (alpha smooth muscle actin) staining and (A, *ii*) maximum tunica media thickness quantification. Masson's Trichrome (B) staining and (C) quantification. (D) Verhoeff van Gieson staining (elastin; yellow arrows indicate elastin fibrils or fibers). Boxes in the low-magnification images (A, *i*, Left; B, Left; and D, Left) indicate the high-magnification images (A, *i*, Right; B, Right; and D, Right) locations ($n = 3-6$). (Scale bars: A, *i*, Left; B, Left; and D, Left, 200 μm ; A, *i*, Right; B, Right; and D, Right, 30 μm .) * $P < 0.05$; ** $P \leq 0.01$; **** $P \leq 0.0001$; $\Delta P \leq 0.07$. (E) Longitudinal sections of 24-wk acellular sdVGs from the proximal to the distal native aorta (Ao) stained for (i) SMCs and (ii) Masson's Trichrome. Boxes in the low-magnification images (Left) indicate the high-magnification image (Right) locations. Black arrows indicate anastomoses. (Scale bars: E, Left, 300 μm ; E, Right, 30 μm .) For all images, lumen (L), PCL sheath (P), and fibrin (F) are indicated. (Scale bars: D, Left, 300 μm ; D, Right, 30 μm .)

circumferential SMCs in the tunica media layer at week 24 is highly similar to the native abdominal aorta, indicating healthy and functional neotissue formation. Furthermore, the endothelialization appears to increase medial layer formation at 8 wk, which suggests that endothelialization yields more positive remodeling toward a native-like structure and results in an sdVG with a bioactive effect.

Conclusion

This study established a fibrin fiber-based acellular off-the-shelf and endothelialized bioactive sdVG. We designed and optimized a hollow fibrin microfiber tube with controlled surface topography via electromechanical stretching, enabling immediate perfusion both in vitro and in vivo, and formation of a confluent endothelium, similar to the native tunica intima. Initial mechanical failure of the natural polymer sdVGs within 1–10 d in vivo due to tearing from the anastomosis was resolved by increased cross-linking and addition of an ultrathin PCL sheath as a surgical intervention to improve suturability. These grafts could be fabricated and endothelialized with ECFCs to produce a bioactive sdVG within 1 wk, a clinically and commercially relevant timeline. The extended implantation of these sdVGs for up to 24 wk indicates that the durable, hybrid sdVG overcame several limitations of natural polymer sdVGs while still enabling regeneration of the healing artery. These sdVGs are able to maintain functionality as an arterial conduit exposed to high pulsatile pressure for over 24 wk in vivo. Mechanical properties of the implanted fibrin–PCL sdVGs closely approximate the native abdominal aorta properties after just 1 wk in vivo and do not lead to changes in arterial resistivity and pulsatility. Elasticity of the harvested endothelialized sdVGs is more consistent with the native abdominal aorta. These mechanical changes were due to host cells extensively remodeling the fibrin, leading to the formation of a mature vascular structure composed of a tunica media containing SMCs, collagen, and elastin as well as a confluent intimal layer of ECs. Interestingly, despite prior endothelialization of bioactive grafts, a complete tunica intima was not present in vivo at week 1, and the disappearance of implanted cells by week 1 remains a concern for clinical translation. The cellular and ECM immunohistochemistry analyses at multiple early and long-term time points may help elucidate the “largely unclear” mechanism of graft remodeling (22), indicating the potentially prolonged role of mature macrophages on scaffold remodeling, the stable tunica intima and media being formed by 4 wk, and the abundant deposition and organiza-

tion of ECM from 4 to 24 wk. This process should be confirmed in an immunocompetent mouse model. The fibrin structure, not the PCL sheath, remodeled to more closely resemble the native abdominal aorta. Despite an acute presence in the implanted sdVG, ECFCs reduced calcification at later time points, accelerated tunica media formation, and controlled healthy remodeling via delayed and reduced macrophage infiltration and vasa vasorum-like structure formation. The fibrin microfiber inner layer mediated the formation of a healthy, mature vascular phenotype, while the progenitor ECs provided a bioactive effect to enhance neotissue formation.

Using enhanced microtopography configurations of cross-linked fibrin tubes and an ultrathin PCL sheath as a surgical intervention, we are able to overcome the mechanical property deficiencies of natural polymer-derived sdVGs while providing the regenerative capacity of the solely natural polymer-based scaffolds. This work advances the sdVG field by utilizing a controlled natural polymer electrospinning process to first create organized and multilayered natural polymer scaffolds for enhanced remodeling compared with the random structure created via molding and most electrospinning techniques (24, 27–29, 31, 32, 71, 72). Importantly, our clinically and commercially relevant sdVG design affords the flexibility to create both off-the-shelf acellular and bioactive endothelialized grafts, depending on the application, within 1 wk. This short fabrication process for acellular and bioactive sdVGs yields significant elastogenesis in vivo, which has previously taken several months of preculturing cells on the scaffolds to achieve (24, 31, 40). Our sdVG matches the native vessel size and mechanical properties, incorporated into the native vascular tissue, and had low thrombogenicity, fulfilling many of the requirements that would benefit arterial bypass patients. Overall, the patency and positive remodeling of the sdVGs in vivo over 24 wk offer a promising technology for arterial bypass procedures and warrant additional investigation.

Materials and Methods

Detailed materials and methods are provided in *SI Appendix, Materials and Methods*.

Preparation of Fibrin Hydrogel Microfiber Tubes and PCL Sheaths. Fibrin hydrogel microfiber sheets were prepared by electrospinning 2.0 wt % fibrinogen codissolved in 0.2 wt % polyethylene oxide onto a grounded, rotating collection bath containing 50 mM calcium chloride and 20 U/mL thrombin as previously described (41–43). The landing position of the spinning jet was

rastered back and forth to yield a uniform aligned fibrin sheet, which was rolled onto a PTFE-coated mandrel. Fibrin tubes were either cross-linked in 100 U/mL thrombin for 2 h before lyophilization or cross-linked in 40 mM EDC/100 mM NHS in PBS for 15 h before dehydration via graded EtOH treatment. Fibrin tubes were stored at 4 °C and rehydrated in 75% EtOH and deionized (DI) H₂O with 1% penicillin/streptomycin before use.

PCL sheaths were prepared by electrospinning 16% (wt/vol) PCL with an 85:15 ratio of low-molecular weight:high-molecular weight PCL codissolved in 10% (wt/vol) dimethylformamide and 90% (wt/vol) dichloromethane onto a grounded, rotating 2.0-mm mandrel. The needle was rastered back and forth. The sheaths had 30- to 50- μ m-thick walls and were fitted to the fibrin microfiber tubes, which was critical for implantation, by heat treatment in 50 °C DI H₂O for 5 min and 54 °C DI H₂O for 1 min.

Graft Analysis. For scanning electron microscopy (SEM), dried fibrin tubes were sputter coated with Au/Pd and imaged using a JEOL 6700F field emission electron microscope. Mechanical testing for elastic modulus, axial STF, and axial UTS was done using a Q800 DMA under tensile loading conditions in controlled ramp force mode (rate: 0.05 N/min, preload force: 0.001 N) until tube failure. To determine circumferential UTS and STF, the sample was mounted radially onto a DMT560 electromechanical puller and subjected to radial stress (rate: 50 μ m/s) until failure (73, 74). Using the DMT560, we determined ultimate SRS by axially pulling (rate: 100 μ m/s) 10–0 nylon sutures placed through one wall at a distance of 2 mm from the graft end and looped over a puller pin. Burst pressure and passive compliance were measured using pressure myography (DMT) as previously (24, 73–79).

Perfusion and Cellularization of Fibrin Microfiber Tubes. A sterilized LumeGen single-chamber bioreactor system was used (Bangalore Integrated System Solutions Ltd.) (80–82) for pulsatile perfusion of fibrin tubes secured in place using 6–0 sutures. A blue dye (dye concentration: 6.78 ppm) was flowed through the graft for 24 h, while clear PBS was used to fill the chamber. The shear stress was set to 7 dyn/cm² (flow rate: ~5 mL/h, pulsatile pressure: 5/4 mmHg) or 14 dyn/cm² (flow rate: ~11 mL/h, pulsatile pressure: 8/5 mmHg) to simulate physiologic conditions. Spectrophotometry was used to determine the chamber absolute dye concentration. Human ECFCs (Lonza), which were cultured as previously described (41, 42), were internally seeded by injecting a suspension of 1.4×10^3 cells per microliter into the fibrin tube. Subsequently, bioreactors were tumbled for 24 h and cultured statically for 3–4 d. For immunofluorescent staining, samples were processed as previously described (41, 42) and imaged using confocal microscopy (LSM 780; Carl Zeiss Inc.).

Implantation of sdVGs. Grafts (length: 3 mm) were implanted as abdominal aorta interposition grafts, as previously described (35, 65), in female Fox Chase SCID Beige mice ($n = 68$, CB17.Cg-Prkdc^{scid}Lyst^{tg-1}/Crl; Charles River) using 10–0 nylon suture for the end-to-end proximal and distal anastomoses. Aspirin (30 mg/L; Bayer) in their drinking water was administered at a dose of 3–4 mg/kg per day to prevent excess graft thrombosis from the time of graft implant to harvest (83).

Blood Flow Measurements. Blood flow profiles of the native abdominal aorta and implanted sdVG were monitored using moorFLPI speckle contrast imager as previously described (84–86). Measurements were taken immediately postimplantation and before harvest while the mice were anesthetized and normalized to preimplant measurements.

Graft patency and blood flow were measured in unsedated mice using the Vevo 2100 ultrasound system equipped with a 40-MHz transducer at baseline and postimplantation. Using color Doppler, the abdominal aorta and grafts were visualized in B mode. In the distal abdominal aorta, a sample pulse wave spectral Doppler was collected (sweep: 200 mm/s) and analyzed for PSV, EDV, MV, RI, and PI (21, 87).

Staining and Quantification. After harvesting the graft, the anastomosed artery and sdVG were flushed with a saline–heparin solution by inserting a needle into the native vessel. The proximal abdominal aorta and one-half of the sdVGs underwent circumferential mechanical testing as above. The distal one-half was fixed in 10% formalin, sectioned cross-sectionally, and stained. Alternatively, the graft anastomosed to the proximal and distal artery was longitudinally sectioned for a continuous view of neotissue formation. Hematoxylin and eosin, Masson's Trichrome, Verhoeff van Gieson, and von Kossa staining was performed by the Johns Hopkins University Oncology Tissue Services and Reference Histology Cores. Immunohistochemistry staining was performed as previously described (84) and imaged with an upright light microscope (Nikon Accuscope 3000, DS-F12). For analysis, three to eight different sections per condition and per time point were sampled. Image analyses were performed using Image J (NIH), MatLab (MathWorks), or Python. TELI-FISH was performed by Alan Meeker's laboratory at Johns Hopkins University School of Medicine as in their previous work (64).

Statistical Analysis. All experiments were performed for at least three biological replicates as detailed throughout the figures. Statistical analysis was performed using GraphPad Prism 7.03. Unpaired *t* tests, one-way ANOVA with Tukey's posttest, or two-way ANOVA with Tukey's or Sidak's posttest were used where appropriate. Unless otherwise indicated, graphical data were reported as mean \pm SD.

ACKNOWLEDGMENTS. We appreciate the assistance of Dr. Hiroshi Matsushita with surgery; Savannah Est with *in vivo* preparation; Dr. Hawley Pruitt and Eugenia Volkova with immunohistochemistry; Calvin Chang with PCL electrospinning; Dr. Alan Meeker with TELI-FISH; Marcel Rauer, Sean Melucci, James Chen, and Melissa Jones with mechanical testing; Dr. Quinton Smith with MatLab coding; Dr. Sebastian Barreto-Ortiz, Michael Blatchley, and Dr. Daniel Lewis with scientific discussions; Jessica Shen, Nicholas Malloy, and Elaine Nagahara with histology imaging; and Khyati Prasad with ultrasound measurements. This work was supported by the shared resources from the Sydney Kimmel Cancer Center, Johns Hopkins University Grant P30 CA006973, NSF Graduate Research Fellowship Program 2015 Fellowship (to M.B.E.), NSF Grant DMR1410240 (to H-Q.M.), Maryland Stem Cells Research Fund Grant MSCRFI-2017 (to H-Q.M., N.H., and S.G.), National Cancer Institute Physical Sciences–Oncology Center Grant U54CA210173 (to S.G.), and American Heart Association Established Investigator Award 15EIA22530000 (to S.G.).

1. L. Gui, A. Muto, S. A. Chan, C. K. Breuer, L. E. Niklason, Development of decellularized human umbilical arteries as small-diameter vascular grafts. *Tissue Eng. Part A* **15**, 2665–2676 (2009).
2. S. Sundaram, A. Echter, A. Sivarapatna, C. Qiu, L. Niklason, Small-diameter vascular graft engineered using human embryonic stem cell-derived mesenchymal cells. *Tissue Eng. Part A* **20**, 740–750 (2014).
3. C. A. Thompson *et al.*, A novel pulsatile, laminar flow bioreactor for the development of tissue-engineered vascular structures. *Tissue Eng.* **8**, 1083–1088 (2002).
4. D. Mozaffarian *et al.*; American Heart Association Statistics Committee and Stroke Statistics Subcommittee, Heart disease and stroke statistics—2015 update: A report from the American heart association. *Circulation* **131**, e29–e322 (2015).
5. J. T. Patterson *et al.*, Tissue-engineered vascular grafts for use in the treatment of congenital heart disease: From the bench to the clinic and back again. *Regen. Med.* **7**, 409–419 (2012).
6. C. L. Webb *et al.*; Congenital Cardiac Defects Committee of the American Heart Association Section on Cardiovascular Disease in the Young, Collaborative care for adults with congenital heart disease. *Circulation* **105**, 2318–2323 (2002).
7. M. S. Connelly *et al.*, Canadian consensus conference on adult congenital heart disease 1996. *Can. J. Cardiol.* **14**, 395–452 (1998).
8. I. Adachi *et al.*, Fontan operation with a viable and growing conduit using pedicled autologous pericardial roll: Serial changes in conduit geometry. *J. Thorac. Cardiovasc. Surg.* **130**, 1517–1522.e1 (2005).
9. R. K. Woods, U. Dyamenahalli, B. W. Duncan, G. L. Rosenthal, F. M. Lupinetti, Comparison of extracardiac Fontan techniques: Pedicled pericardial tunnel versus conduit reconstruction. *J. Thorac. Cardiovasc. Surg.* **125**, 465–471 (2003).
10. N. D. Desai, E. A. Cohen, C. D. Naylor, S. E. Fremes; Radial Artery Patency Study Investigators, A randomized comparison of radial-artery and saphenous-vein coronary bypass grafts. *N. Engl. J. Med.* **351**, 2302–2309 (2004).
11. A. E. van den Bosch *et al.*, Long-term outcome and quality of life in adult patients after the Fontan operation. *Am. J. Cardiol.* **93**, 1141–1145 (2004).
12. Y.-U. Lee *et al.*, Implantation of inferior vena cava interposition graft in mouse model. *J. Vis. Exp.*, e51632 (2014).
13. J. E. Mayer, Jr, *et al.*, Factors associated with marked reduction in mortality for Fontan operations in patients with single ventricle. *J. Thorac. Cardiovasc. Surg.* **103**, 444–451 (1992).
14. L. Buttafoco *et al.*, Physical characterization of vascular grafts cultured in a bioreactor. *Biomaterials* **27**, 2380–2389 (2006).
15. X. Zhang *et al.*, Dynamic culture conditions to generate silk-based tissue-engineered vascular grafts. *Biomaterials* **30**, 3213–3223 (2009).
16. C. Williams, T. M. Wick, Perfusion bioreactor for small diameter tissue-engineered arteries. *Tissue Eng.* **10**, 930–941 (2004).
17. T. Neumann, B. S. Nicholson, J. E. Sanders, Tissue engineering of perfused microvessels. *Microvasc. Res.* **66**, 59–67 (2003).
18. M. S. Hahn, M. K. McHale, E. Wang, R. H. Schmedlen, J. L. West, Physiologic pulsatile flow bioreactor conditioning of poly(ethylene glycol)-based tissue engineered vascular grafts. *Ann. Biomed. Eng.* **35**, 190–200 (2007).
19. S. de Valence *et al.*, Long term performance of polycaprolactone vascular grafts in a rat abdominal aorta replacement model. *Biomaterials* **33**, 38–47 (2012).
20. H. Kurobe *et al.*, Development of small diameter nanofiber tissue engineered arterial grafts. *PLoS One* **10**, e0120328 (2015).
21. L. E. Niklason *et al.*, Functional arteries grown *in vitro*. *Science* **284**, 489–493 (1999).

22. S. Pashneh-Tala, S. MacNeil, F. Claeysens, The tissue-engineered vascular graft-past, present, and future. *Tissue Eng. Part B Rev.* **22**, 68–100 (2016).
23. M. B. Elliott, S. Gerecht, Three-dimensional culture of small-diameter vascular grafts. *J. Mater. Chem. B Mater. Biol. Med.* **4**, 3443–3453 (2016).
24. L. Gui *et al.*, Construction of tissue-engineered small-diameter vascular grafts in fibrin scaffolds in 30 days. *Tissue Eng. Part A* **20**, 1499–1507 (2014).
25. L. Gui *et al.*, Implantable tissue-engineered blood vessels from human induced pluripotent stem cells. *Biomaterials* **102**, 120–129 (2016).
26. J. H. Lawson *et al.*, Bioengineered human acellular vessels for dialysis access in patients with end-stage renal disease: Two phase 2 single-arm trials. *Lancet* **387**, 2026–2034 (2016).
27. D. D. Swartz, J. A. Russell, S. T. Andreadis, Engineering of fibrin-based functional and implantable small-diameter blood vessels. *Am. J. Physiol. Heart Circ. Physiol.* **288**, H1451–H1460 (2005).
28. T. Aper *et al.*, Novel method for the generation of tissue-engineered vascular grafts based on a highly compacted fibrin matrix. *Acta Biomater.* **29**, 21–32 (2016).
29. J. L. Long, R. T. Tranquillo, Elastic fiber production in cardiovascular tissue-equivalents. *Matrix Biol.* **22**, 339–350 (2003).
30. J. Johnson, D. Ohst, T. Groehl, S. Hettterscheidt, M. Jones, Development of novel, bioresorbable, small-diameter electrospun vascular grafts. *J. Tissue Sci. Eng.* **6**, 1000151 (2015).
31. Z. Syedain *et al.*, Tissue engineering of acellular vascular grafts capable of somatic growth in young lambs. *Nat. Commun.* **7**, 12951 (2016).
32. Z. H. Syedain *et al.*, A completely biological “off-the-shelf” arteriovenous graft that recellularizes in baboons. *Sci. Transl. Med.* **9**, ean4209 (2017).
33. N. J. Kristofik *et al.*, Improving in vivo outcomes of decellularized vascular grafts via incorporation of a novel extracellular matrix. *Biomaterials* **141**, 63–73 (2017).
34. W. Gong *et al.*, Hybrid small-diameter vascular grafts: Anti-expansion effect of electrospun poly ϵ -caprolactone on heparin-coated decellularized matrices. *Biomaterials* **76**, 359–370 (2016).
35. T. Fukunishi *et al.*, Tissue-engineered small diameter arterial vascular grafts from cell-free nanofiber PCL/chitosan scaffolds in a sheep model. *PLoS One* **11**, e0158555 (2016).
36. Y. M. Ju *et al.*, Electrospun vascular scaffold for cellularized small diameter blood vessels: A preclinical large animal study. *Acta Biomater.* **59**, 58–67 (2017).
37. C. E. Schmidt, J. M. Baier, Acellular vascular tissues: Natural biomaterials for tissue repair and tissue engineering. *Biomaterials* **21**, 2215–2231 (2000).
38. C. L. Cummings, D. Gawlitta, R. M. Nerem, J. P. Stegemann, Properties of engineered vascular constructs made from collagen, fibrin, and collagen-fibrin mixtures. *Biomaterials* **25**, 3699–3706 (2004).
39. S. Row *et al.*, Arterial grafts exhibiting unprecedented cellular infiltration and remodeling in vivo: The role of cells in the vascular wall. *Biomaterials* **50**, 115–126 (2015).
40. S. Koch *et al.*, Fibrin-poly(lactide)-based tissue-engineered vascular graft in the arterial circulation. *Biomaterials* **31**, 4731–4739 (2010).
41. S. F. Barreto-Ortiz *et al.*, Fabrication of 3-dimensional multicellular microvascular structures. *FASEB J.* **29**, 3302–3314 (2015).
42. S. F. Barreto-Ortiz *et al.*, A novel in vitro model for microvasculature reveals regulation of circumferential ECM organization by curvature. *PLoS One* **8**, e81061 (2013).
43. S. Zhang *et al.*, Creating polymer hydrogel microfibrils with internal alignment via electrical and mechanical stretching. *Biomaterials* **35**, 3243–3251 (2014).
44. M. Davenport, “VEGF bound to heparin-conjugated, electrospun fibrin microfibril supports ECM formation and orientation on 3d, in vitro microvascular model,” MS thesis, Johns Hopkins University, Baltimore (2014).
45. P. Thevenot, W. Hu, L. Tang, Surface chemistry influences implant biocompatibility. *Curr. Top. Med. Chem.* **8**, 270–280 (2008).
46. Q. Smith *et al.*, Differential HDAC6 activity modulates ciliogenesis and subsequent mechanosensing of endothelial cells derived from pluripotent stem cells. *Cell Rep.* **24**, 895–908.e6 (2018).
47. X. Chen, D. Gays, C. Milia, M. M. Santoro, Cilia control vascular mural cell recruitment in vertebrates. *Cell Rep.* **18**, 1033–1047 (2017).
48. T. G. Papaioannou, C. Stefanadis, Vascular wall shear stress: Basic principles and methods. *Hellenic J. Cardiol.* **46**, 9–15 (2005).
49. H. E. Abaci, R. Devendra, R. Soman, G. Drazer, S. Gerecht, Microbioreactors to manipulate oxygen tension and shear stress in the microenvironment of vascular stem and progenitor cells. *Biotechnol. Appl. Biochem.* **59**, 97–105 (2012).
50. M. Tsai *et al.*, In vitro modeling of the microvascular occlusion and thrombosis that occur in hematologic diseases using microfluidic technology. *J. Clin. Invest.* **122**, 408–418 (2012).
51. I. S. Anand, Hypoxia and the pulmonary circulation. *Thorax* **49** (suppl.), S19–S24 (1994).
52. F. E. Rey, M. E. Cifuentes, A. Kiarash, M. T. Quinn, P. J. Pagano, Novel competitive inhibitor of NAD(PH) oxidase assembly attenuates vascular O₂(-) and systolic blood pressure in mice. *Circ. Res.* **89**, 408–414 (2001).
53. A. Yahyouché, X. Zhidao, J. T. Czernuszka, A. J. P. Clover, Macrophage-mediated degradation of crosslinked collagen scaffolds. *Acta Biomater.* **7**, 278–286 (2011).
54. J. McDowall, “Fibrinogen” in *Protein of the Month*. https://www.ebi.ac.uk/interpro/potm/2006_11/Page1.htm. Accessed 14 April 2019.
55. T. A. E. Ahmed, E. V. Dare, M. Hincke, Fibrin: A versatile scaffold for tissue engineering applications. *Tissue Eng. Part B Rev.* **14**, 199–215 (2008).
56. X. Li, J. Xu, C. T. Nicolescu, J. T. Marinelli, J. Tien, Generation, endothelialization, and microsurgical suture anastomosis of strong 1-mm-diameter collagen tubes. *Tissue Eng. Part A* **23**, 335–344 (2017).
57. V. W. van Hinsbergh, Endothelium: Role in regulation of coagulation and inflammation. *Semin. Immunopathol.* **34**, 93–106 (2012).
58. E. J. Brisbois *et al.*, Reduction in thrombosis and bacterial adhesion with 7 day implantation of S-nitroso-N-acetylpenicillamine (SNAP)-doped Elast-eon E2As catheters in sheep. *J. Mater. Chem. B Mater. Biol. Med.* **3**, 1639–1645 (2015).
59. P. S. Fleser *et al.*, Nitric oxide-releasing biopolymers inhibit thrombus formation in a sheep model of arteriovenous bridge grafts. *J. Vasc. Surg.* **40**, 803–811 (2004).
60. T. Asahara *et al.*, Isolation of putative progenitor endothelial cells for angiogenesis. *Science* **275**, 964–967 (1997).
61. D. A. Ingram *et al.*, Identification of a novel hierarchy of endothelial progenitor cells using human peripheral and umbilical cord blood. *Blood* **104**, 2752–2760 (2004).
62. M. J. Javed *et al.*, Endothelial colony forming cells and mesenchymal stem cells are enriched at different gestational ages in human umbilical cord blood. *Pediatr. Res.* **64**, 68–73 (2008).
63. G. König *et al.*, Mechanical properties of completely autologous human tissue engineered blood vessels compared to human saphenous vein and mammary artery. *Biomaterials* **30**, 1542–1550 (2009).
64. D. J. Vander Griend, Y. Konishi, A. M. De Marzo, J. T. Isaacs, A. K. Meeker, Dual-label centromere and telomere FISH identifies human, rat, and mouse cell contribution to multiplexes recombinant urogenital sinus xenografts. *Prostate* **69**, 1557–1564 (2009).
65. N. Hibino *et al.*, Evaluation of the use of an induced pluripotent stem cell sheet for the construction of tissue-engineered vascular grafts. *J. Thorac. Cardiovasc. Surg.* **143**, 696–703 (2012).
66. S. Kaushal *et al.*, Functional small-diameter neovessels created using endothelial progenitor cells expanded ex vivo. *Nat. Med.* **7**, 1035–1040 (2001).
67. N. Hibino *et al.*, Tissue-engineered vascular grafts form neovessels that arise from regeneration of the adjacent blood vessel. *FASEB J.* **25**, 2731–2739 (2011).
68. S. Tara *et al.*, Well-organized neointima of large-pore poly(L-lactic acid) vascular graft coated with poly(L-lactic-co- ϵ -caprolactone) prevents calcific deposition compared to small-pore electrospun poly(L-lactic acid) graft in a mouse aortic implantation model. *Atherosclerosis* **237**, 684–691 (2014).
69. S. Row, D. D. Swartz, S. T. Andreadis, Animal models of cardiovascular disease as test beds of bioengineered vascular grafts. *Drug Discov. Today Dis. Models* **24**, 37–45 (2017).
70. S. R. Caliari, J. A. Burdick, A practical guide to hydrogels for cell culture. *Nat. Methods* **13**, 405–414 (2016).
71. W. He *et al.*, Pericyte-based human tissue engineered vascular grafts. *Biomaterials* **31**, 8235–8244 (2010).
72. P. C. Caracciolo *et al.*, Surface-modified bioresorbable electrospun scaffolds for improving hemocompatibility of vascular grafts. *Mater. Sci. Eng. C* **75**, 1115–1127 (2017).
73. S. M. Jung *et al.*, Increased tissue transglutaminase activity contributes to central vascular stiffness in eNOS knockout mice. *Am. J. Physiol. Heart Circ. Physiol.* **305**, H803–H810 (2013).
74. J. Steppan *et al.*, Exercise, vascular stiffness, and tissue transglutaminase. *J. Am. Heart Assoc.* **3**, e000599 (2014).
75. L. Santhanam *et al.*, Inducible NO synthase dependent S-nitrosylation and activation of arginase1 contribute to age-related endothelial dysfunction. *Circ. Res.* **101**, 692–702 (2007).
76. L. Santhanam *et al.*, Decreased S-nitrosylation of tissue transglutaminase contributes to age-related increases in vascular stiffness. *Circ. Res.* **107**, 117–125 (2010).
77. K. G. Soucy *et al.*, Single exposure gamma-irradiation amplifies xanthine oxidase activity and induces endothelial dysfunction in rat aorta. *Radiat. Environ. Biophys.* **46**, 179–186 (2007).
78. A. R. White *et al.*, Knockdown of arginase I restores NO signaling in the vasculature of old rats. *Hypertension* **47**, 245–251 (2006).
79. A. R. White *et al.*, Early changes in vasoreactivity after simulated microgravity are due to an upregulation of the endothelium-dependent nitric oxide/cGMP pathway. *Eur. J. Appl. Physiol.* **110**, 395–404 (2010).
80. H. Peng, E. M. Schlaich, S. Row, S. T. Andreadis, D. D. Swartz, A novel ovine ex vivo arteriovenous shunt model to test vascular implantability. *Cells Tissues Organs* **195**, 108–121 (2012).
81. M. Y. Tondreau *et al.*, Mechanical properties of endothelialized fibroblast-derived vascular scaffolds stimulated in a bioreactor. *Acta Biomater.* **18**, 176–185 (2015).
82. S. E. McIlhenny *et al.*, Linear shear conditioning improves vascular graft retention of adipose-derived stem cells by upregulation of the $\alpha 5 \beta 1$ integrin. *Tissue Eng. Part A* **16**, 245–255 (2010).
83. T. Cyrus *et al.*, Effect of low-dose aspirin on vascular inflammation, plaque stability, and atherogenesis in low-density lipoprotein receptor-deficient mice. *Circulation* **106**, 1282–1287 (2002).
84. Y.-I. Shen *et al.*, Engineered human vascularized constructs accelerate diabetic wound healing. *Biomaterials* **102**, 107–119 (2016).
85. Y.-I. Shen *et al.*, Acellular hydrogels for regenerative burn wound healing: Translation from a porcine model. *J. Invest. Dermatol.* **135**, 2519–2529 (2015).
86. G. Sun *et al.*, Dextran hydrogel scaffolds enhance angiogenic responses and promote complete skin regeneration during burn wound healing. *Proc. Natl. Acad. Sci. U.S.A.* **108**, 20976–20981 (2011).
87. G. B. Chavhan, D. A. Parra, A. Mann, O. M. Navarro, Normal Doppler spectral waveforms of major pediatric vessels: Specific patterns. *Radiographics* **28**, 691–706 (2008).
88. R. Marx *et al.*, Morphological differences of the internal thoracic artery in patients with and without coronary artery disease—Evaluation by duplex-scanning. *Eur. J. Cardiothorac. Surg.* **20**, 755–759 (2001).
89. Z. Teng, D. Tang, J. Zheng, P. K. Woodard, A. H. Hoffman, An experimental study on the ultimate strength of the adventitia and media of human atherosclerotic carotid arteries in circumferential and axial directions. *J. Biomech.* **42**, 2535–2539 (2009).
90. B. A. Hamedani, M. Navidbakhsh, H. A. Tafti, Comparison between mechanical properties of human saphenous vein and umbilical vein. *Biomed. Eng. Online* **11**, 59 (2012).